Problem Analysis and Improvement of Traditional Efficiency Optimization Method for Inductive Power Transfer Systems

Deliang Chen

***Abstract*—Due to the wide range of battery terminal voltage variations caused by the different states of charge of power batteries in electric vehicles, and due to the consideration of interoperability among different vehicle models, inductive wireless charging systems are required to be able to cope with a wide range of voltage conditions to realize high efficiency. Phase shift control is often considered to be an effective means to fulfill this goal. However, traditional optimization methods exclude the zero-voltage-switching (ZVS) constraints from the optimization objective, leading to non-optimal solutions under some operating conditions. Therefore, an optimization method based on the optimal numerical solution, which further exploits the efficiency potential of the system by disregarding the presuppositions about the ac voltage gain in the traditional optimization methods is proposed in this article. As an adjunct, a ZVS realization method considering higher harmonics based on two hybrid phase-shift regulation strategies is also proposed that can be adapted to any reasonable ZVS current setting and achieve more accurate tracking. Afterward, the applicability of the traditional and improved methods is analyzed accordingly, followed by a comparison verification based on a small-scale experimental platform.**

***Index Terms*—Inductive power transfer (IPT), S-S compensated, wide voltage range, zero-voltage-switching (ZVS).**

I. Introduction

INDUCTIVE power transfer (IPT) system has attracted widespread attention in the past decades in case of its flexibility and reliability. As a convenient and safe power transfer approach, the IPT system delivers energy without physical connection [1], avoiding the electrical sparks in the charging process effectively, and it is equipped with strong adaptability to harsh conditions including rain, snow, etc. [2], [3], [4] In recent years, IPT technology has been widely applied in consumer electronics [5], medical devices [6], underwater equipment [7], electric vehicles (EVs) [8], [9], etc.

In practical applications like the EVs charging, the voltage of the battery varies with the charging state, which requires the IPT system to have high efficiency over the wide voltage range [10], [11]. To cope with the aforesaid demands, many solutions have been proposed, which can be divided into two broad categories as shown in Fig. 2. The first type is the multistage solution which installs the extra dc–dc converters on one or two sides of IPT stage [12], [13]. The output power can be flexibly regulated, and the impedance can be easily matched. Accordingly, the efficiency of the resonant tanks is improved. The second type is the single-stage solution without the additional dc–dc converter which is more desirable. The way to continuously tune inductance or capacitance by changing the resonance parameters so that the system impedance can be adapted to different operating conditions is proposed in [14], [15], and [16]. However, these continuously variable components require careful design and are not suitable for high-power applications. While the discrete variation of parameters avoids the aforesaid problems, it needs to configure inductor or capacitor arrays [17], [18] according to the resolution, increasing the cost and volume. Obviously, the retrofit approach by adding circuit elements will increase losses, cost, and hardware volume, whether it is single-stage types or multi-stage types.

On the contrary, the solution by improving the regulation strategy without adding any additional components is more economical and promising. For example, pulse frequency modulation (PFM) is the basic method adopted to attain output regulation by changing the distribution of the equivalent impedance of the IPT system [19]. However, the wide voltage range and power range operating requirement give rise to extremely wide variation of the switching frequency which may exceed the allowed range for EVs (79–90 kHz), and it also may cause a frequency bifurcation phenomenon. These problems can be well averted by the phase shift modulation (PSM) scheme, as shown in Fig. 1. Typically, the free control variables of PSM include the respective inner phase shift angles α, β of the primary and

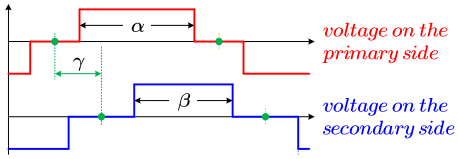

Fig. 1. Schematic diagram of PSM.

Received 15 April 2024; revised 28 June 2024; accepted 28 July 2024. Date of publication 2 August 2024; date of current version 26 February 2025. This work was supported in part by the National Natural Science Foundation of Shandong Province under Grant ZR2024QE428. Recommended for publication by Associate Editor J. Acero.

The author is with the Shandong University, Jinan 250061, China (e-mail: chendeliang@sdu.edu.cn).

Color versions of one or more figures in this article are available at https://doi.org/10.1109/TPEL.2024.3437782.

Digital Object Identifier 10.1109/TPEL.2024.3437782

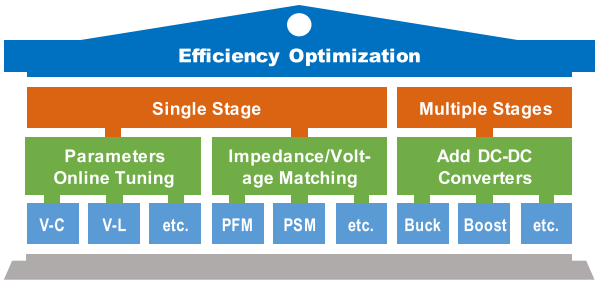

Fig. 2. Some mainstream efficiency optimization methods for IPT systems (V-C: variable capacitance and V-L: variable inductance).

secondary sides, and the outer phase shift angle γ between the primary and secondary sides.

In [20], a dual inner PSM strategy for S-S compensated dual-active IPT system by setting the fundamental current stresses on both sides to be equal and $\gamma = \frac{\pi}{2}$ is proposed, thus balancing the losses on the primary and secondary sides, but the idea is not suitable to the wide voltage range. In [21], the optimal load of the S-S compensated semi-active rectifier IPT system is determined by ensuring that the secondary voltage and current are always in phase, based on the efficiency estimation equation. Subsequently, the coupling relationship between α, β, and the dc voltage gain is established by equating the power on the fundamental equivalent resistor to the actual power, resulting in the decoupling of the optimal efficiency with the load and mutual inductance. Thereafter, the closed-loop control and the optimal efficiency tracking are achieved with the cooperation of the perturbation and observation (P&O) method. The limitation, however, lies in its restriction on the properties of the circuit on the secondary side without taking into account the phase state of the primary side. Similarly, in [22], the law governing the optimal efficiency of the S-S compensated dual-active IPT system's fundamental ac voltage gain is determined by setting $\gamma = \frac{\pi}{2}$, and maximum efficiency tracking is performed by P&O. Jiang et al. [23], [24] provide a detailed analysis of the optimal Ohmic losses in IPT systems with SS compensation considering ZVS. However, their analysis model overlooks the impact of higher order harmonics, and the output regulation relies on three independent control loops, which increases the complexity of loop design and implementation.

The current dominant approaches for efficiency optimization based on regulation strategies are impedance matching [21] and voltage gain matching [22], which have been regarded as essentially equivalent according to [25]. However, the issue of zero-voltage-switching (ZVS) has not yet been addressed in [20], [21], [22], and [21]. Therefore, a more sophisticated ZVS analysis method based on differential equations for dual-side *LCC* compensated dual-active IPT system under triple-phase-shift (TPS) is proposed in [25], and subsequently, the required offset of γ to satisfy the ZVS condition is determined. Nevertheless, this analysis method is solely applicable to high-order networks with prominent low-pass filtering characteristics. In [26], a similar mean is attempted to accurately solve the ZVS condition for an S-S compensated dual-active IPT system under TPS modulation. However, the necessity of employing a differential-based solution method is diminished due to treating the high-frequency voltage on the primary side as a sinusoidal waveform and neglecting higher harmonics. A closed-loop control method in [27] combines TPS and PFM to achieve ZVS and maximum efficiency tracking is proposed for S-S compensated dual-active IPT system, but the determination of the control variables relies on a look-up table, which compromises the generality of the control method. A mode switching based method, including full bridge—full bridge (FBFB), full bridge—half bridge (FBHB), half bridge—full bridge (HBFB), and half bridge—half bridge (HBHB), is discussed in [28], which effectively improves the efficiency of the system.

Notwithstanding the effectiveness of the previous work, none of them departs from the most basic means of optimization introduced in [21] and [22]. However, as points out in [29] from the perspective of equation invariance that the aforesaid conclusion of voltage gain matching is not applicable to a wide voltage range, and the essential reason is that the coupling between free variables is ignored. In addition, the ZVS condition is usually treated as an additional independent objective rather than a constraint of the optimal regulation strategy in the derivation of the optimal matching voltage and the optimal matching load. The above two reasons lead to the nonoptimal operation trajectory under some operating conditions. Therefore, Li et al. [29] proposes a segmented TPS strategy with different voltage gain based on an S-S compensated dual-active IPT system, however, its ZVS analysis process is only constrained by the current polarity, which fails to ensure the effective relation of ZVS.

Motivated by these issues, this article will delve further into exploring the potential for efficiency improvement in traditional method based on ac voltage gain. The contributions of this article are as follows.

1) Analysis and elucidation of the flaws and shortcomings in the traditional efficiency optimization method based on ac voltage gain.
2) Based on numerical optimal solutions, summarizing the working states under buck mode operation, a method combining DPS and extended-phase-shift (EPS) regulation to approximate the numerical optimal trajectory is proposed, breaking through the constraints of traditional methods on ac voltage gain. The analysis and execution process of this method provide a new optimization idea for other types of circuit topologies and operating conditions;
3) Taking into account the impact of higher harmonics on ZVS, deriving an executable formula that can more accurately track the ZVS current settings. This method can achieve tracking of any reasonably set ZVS current.

Although the efficiency improvement is not prominent in the experimental validation, there is a strong potential for operational economics after scaling up the application.

The rest of this article is organized as follows. The topology and the working principles are descripted in Section II. The modulation and control strategies are given in Section III. Section IV provides the experimental verifications. Finally, Section V concludes this article.

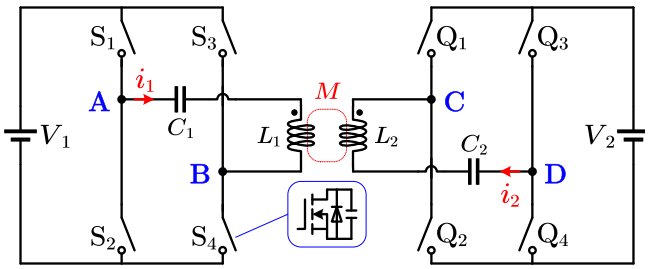

Fig. 3. Topology of SS compensated dual-active IPT system.

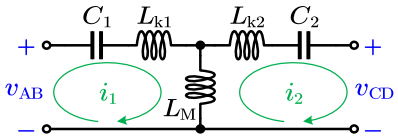

Fig. 4. Equivalent circuit of the S-S compensated network.

II. Topology and the Performances

A. Topology Structure

Since the circuit structure of the S-S compensated IPT system is the simplest and is widely employed in high-power applications, it is used as an example to illustrate the working principle, and its circuit structure is shown in Fig. 3. L_1 and L_2 are the self-inductance of the magnetic coupler, and the turns ratio is N, which is set to one in this article. M is the mutual inductance, and $k = M/\sqrt{L_1 L_2}$ is denoted as the coupling coefficient. C_1 and C_2 are the capacitances to compensate the phase legging of current on the both sides causing by large values of L_1, L_2, and small k. $S_1 \sim S_4$, and $Q_1 \sim Q_4$ are the SiC MOSFETs constituting the high frequency active H-bridge on the both sides. V_1 is the power source supported by a fixed voltage supply, or an end voltage regulator like a Power Factor Correction (PFC), whose value is normally 400 V. V_2 is the load voltage, which is usually a battery. The positive direction of current is highlighted in red in Fig. 3. Since the circuit structure is completely symmetric, only the case of buck forward power flow ($G = V_2/V_1 < 1$, and the power is transferred from V_1 to V_2) is considered in this article to save space, and the other cases can be replicated analogously to the analytical method and flow in this article.

For convenience, the ratios of α, β, and γ to 2π are denoted as d_α, d_β, and d_γ, respectively. Fig. 4 illustrates the T-type equivalent circuit of Fig. 3, where $L_M = k \cdot L_1$, $L_{k1} = L_{k2} = (1-k) \cdot L_1$. The switching frequency f_S is set to the resonant frequency f_R of the network as

$$f_S = f_R = \frac{1}{2\pi\sqrt{L_1 C_1}} = \frac{1}{2\pi\sqrt{L_2 C_2}}. \tag{1}$$

Unless otherwise specified, the following assumptions run through the analysis processes of the full paper.

1) All the switches, inductors, capacitors are ideal.
2) The impact of deadtime is negligible.

B. System Modeling Considering Higher Harmonics

If the moment when the rising edge of v_{AB} (0 to V_1) is taken as the starting point (see Fig. 1), the expressions of v_{AB} and v_{CD} of the S-S compensated IPS system with higher harmonics can be formed as per the Fourier decomposition as

$$\begin{cases} v_{AB} = \sum_{n=1}^{\infty} v_{AB.n} \\ v_{CD} = \sum_{n=1}^{\infty} v_{CD.n} \end{cases} \tag{2}$$

where $\theta_t = \omega_S\, t + \pi(\frac{1}{2} - d_\alpha)$, $\omega_S = 2\pi f_S$, $\varphi_\gamma = -2\pi d_\gamma$,

$$v_{AB.n} = (-1)^{\frac{n-1}{2}} \cdot \frac{4V_1}{n\pi} \cdot \sin(n\pi d_\alpha) \cdot \sin(n\theta_t)$$

$$v_{CD.n} = (-1)^{\frac{n-1}{2}} \cdot \frac{4V_2}{n\pi} \cdot \sin(n\pi d_\beta) \cdot \sin(n\theta_t + n\varphi_\gamma).$$

Then, the mesh currents with higher harmonics in Fig. 4 in accordance with the KCL law are given by

$$\begin{bmatrix} \mathbf{i}_1 \\ \mathbf{i}_2 \end{bmatrix} = \sum_{n=1}^{\infty} \mathrm{j} \cdot a_n \cdot \begin{bmatrix} n^2-1 & kn^2 \\ kn^2 & n^2-1 \end{bmatrix} \begin{bmatrix} \mathbf{v}_{AB.n} \\ -\mathbf{v}_{CD.n} \end{bmatrix} \tag{3}$$

where $\mathbf{i}_1$, $\mathbf{i}_2$, $\mathbf{v}_{AB.n}$, and $\mathbf{v}_{CD.n}$ are vector forms of i_1, i_2, $v_{AB.n}$, and $v_{CD.n}$, respectively. $j^2 = -1$, and

$$a_n = \frac{n}{\omega_S L_1 \cdot (k^2 n^4 - n^4 + 2n^2 - 1)}.$$

Accordingly, the RMS values of (3) are expressed as

$$\begin{cases} i_{1.\mathrm{RMS}}^2 \approx \frac{1}{2}\sum_{n=1}^{\infty} \begin{bmatrix} B_{1.n}^2 + B_{2.n}^2 \\ -2B_{1.n}B_{2.n}\cos(n\varphi_\gamma) \end{bmatrix} \\ i_{2.\mathrm{RMS}}^2 \approx \frac{1}{2}\sum_{n=1}^{\infty} \begin{bmatrix} B_{3.n}^2 + B_{4.n}^2 \\ -2B_{3.n}B_{4.n}\cos(n\varphi_\gamma) \end{bmatrix} \end{cases} \tag{4}$$

$$B_{1.n} = \frac{4a_n}{\pi} \cdot V_1 \cdot \left(n - \frac{1}{n}\right) \cdot |\sin(n\pi d_\alpha)|$$

$$B_{2.n} = \frac{4a_n}{\pi} \cdot V_2 \cdot kn \cdot |\sin(n\pi d_\beta)|$$

$$B_{3.n} = \frac{4a_n}{\pi} \cdot V_1 \cdot kn \cdot |\sin(n\pi d_\alpha)|$$

$$B_{4.n} = \frac{4a_n}{\pi} \cdot V_2 \cdot \left(n - \frac{1}{n}\right) \cdot |\sin(n\pi d_\beta)|.$$

For the output power, only the product of voltage and current of the same order of harmonic is considered, while the product of voltage and current of different order of harmonics can be ignored, and the outcome is

$$P_O = f_S \cdot \int_0^{T_S} v_{AB} \cdot i_1 dt = f_S \cdot \int_0^{T_S} v_{CD} \cdot i_2 dt$$

$$\approx \sum_{n=1}^{\infty} k a_n n^2 V_{AB.n} V_{CD.n} \sin(n\varphi_\gamma) \tag{5}$$

where $T_S = f_S^{-1}$ is the switching period, $V_{AB.n}$ and $V_{CD.n}$ are the magnitudes of $v_{AB.n}$ and $v_{CD.n}$, respectively.

If the turn-ON moments of each switch are distinguished by subscripts, then the ZVS conditions of each switch are found as

$$I_{\mathrm{ZVS}.p} + i_1(t_{S_1}) \le 0, \quad I_{\mathrm{ZVS}.s} - i_2(t_{Q_1}) \le 0$$

$$I_{\mathrm{ZVS}.p} - i_1(t_{S_3}) \le 0, \quad I_{\mathrm{ZVS}.s} + i_2(t_{Q_3}) \le 0$$

where $I_{\text{ZVS}.p}$ and $I_{\text{ZVS}.s}$ are the minimum current to ensure the ZVS operating on the primary and secondary sides, respectively, which can be determined by the junction capacitances and the suffered voltage of each switch as

$$I_{\text{ZVS}.p} = \frac{2C_{\text{oss}.p}V_1}{T_d}, I_{\text{ZVS}.s} = \frac{2C_{\text{oss}.s}V_2}{T_d}$$

where T_d is the dead time, $C_{\text{oss}.p}$ and $C_{\text{oss}.s}$ are the junction capacitances on the primary and secondary sides, respectively. In this article, the switches on the both sides are of the same type, so it can be noted that $I_{\text{ZVS}.p} = I_{\text{ZVS}.s} = I_{\text{ZVS}}$.

Normally, the fundamental component ($n = 1$) of (4) and (5) is sufficient to reflect the operating state of the system, which in turn enables the corresponding optimization and control of the IPT system, but it is not sufficient for ensuring ZVS implementation. Thereby, the resonant current containing the higher harmonics needed to be considered, which is shown in (3).

III. Modulation and Control Strategies

A. Limitations of Traditional Efficiency Optimization

Traditional efficiency optimization methods are based on the predicted efficiency of the IPT system and the process can be briefly described as follows.

Step 1: Based on the fundamental component ($n = 1$) of (3), make $\gamma = \frac{\pi}{2}$ (i.e., $d_\gamma = 0.5$) to achieve zero phase angle at the primary side to reduce the reactive power loss.

Step 2: The sum of the parasitic resistances of the primary and secondary resonant networks and the H-bridge are set to be r_1 and r_2, respectively, to indicate the power losses. Then, the losses of system can be estimated as

$$P_{\text{loss}} = i_{1.\text{RMS}}^2 \cdot r_1 + i_{2.\text{RMS}}^2 \cdot r_2. \tag{6}$$

Accordingly, the efficiency of the IPT system only considering the fundamental component can be estimated as

$$\begin{aligned}\eta_{\text{est}} &= \frac{P_O}{P_O + P_{\text{loss}}} \\ &= \frac{2\omega_S k L_1 G_{\text{AC}} \sin(\gamma)}{2\omega_S k L_1 G_{\text{AC}} \sin(\gamma) + G_{\text{AC}}^2 r_1 + r_2}\end{aligned} \tag{7}$$

where G_{AC} is the ac voltage gain of the resonant network

$$G_{\text{AC}} \triangleq \frac{V_2 \cdot \sin\left(\frac{\beta}{2}\right)}{V_1 \cdot \sin\left(\frac{\alpha}{2}\right)} = \frac{V_2 \cdot \sin(\pi d_\beta)}{V_1 \cdot \sin(\pi d_\alpha)}.$$

Step 3: Consider G_{AC} as the only independent variable of η_{est}, then

$$\frac{\partial \eta_{\text{est}}}{\partial G_{\text{AC}}} = 0 \triangleq \qquad G_{\text{AC}} = \sqrt{\frac{r_2}{r_1}}. \tag{8}$$

If the primary and secondary sides have the same structure and parameters, then $r_1 = r_2$ and $G_{\text{AC}} = 1$ (most literatures adopt this case, namely the turns ratio N of the magnetic coupler $N = 1$).

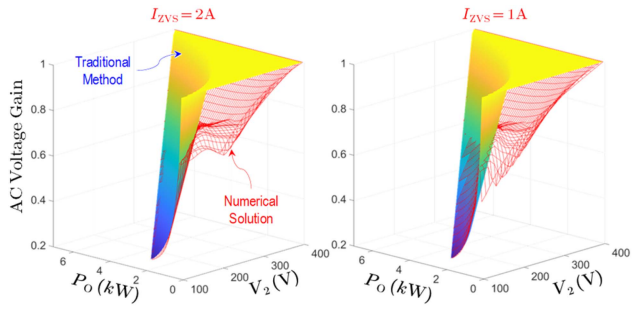

Fig. 5. Comparison of the trends of G_{AC} between the traditional method and the optimal solution at $V_1 = 400$ V, $k = 0.3718$ and $d_{\text{ZVS}} = 0$.

Therefore, the expression for d_β can be derived from the above relationship as

$$d_\beta = \frac{1}{\pi} \cdot \arcsin\left[\frac{V_1}{V_2} \cdot \sin(\pi d_\alpha)\right]. \tag{9}$$

Step 4: To ensure the ZVS of the fundamental component, the outer phase shift angle ratio d_γ needs to satisfy

$$d_\gamma = -\frac{\min(d_\alpha, d_\beta)}{2} + \Delta d_{\text{ZVS}}.$$

According to the phase vector diagram, where Δd_{ZVS} is the ZVS margin angle [25], [28]. When $V_1 > V_2$, the optimized operating condition is $d_\alpha < d_\beta$, so that $d_\gamma = -\frac{d_\alpha}{2}$.

In addition, the values of d_α and d_β need to be limited as

$$0 \le d_\alpha \le 0.5, 0 \le d_\beta \le 0.5.$$

However, the issue with the preceding steps lies in the fact that the ZVS conditions are not incorporated as a constraint within the efficiency optimization process, but rather are treated as an independent execution requirement. This approach undermines the achievement of the extreme value condition deduced from (7).

For an IPT system characterized by identical primary and secondary side configurations, the efficiency optimization challenge can be articulated through the subsequent (10), where f_{cost} is the cost function, which represents the conduction loss of the system, P_{target} is the demanded output power, acting as an equation constraint, while the inequality constraints are ZVS conditions

$$\begin{aligned}\min \quad & f_{\text{cost}} = i_{1.\text{RMS}}^2 + i_{2.\text{RMS}}^2 \\ \text{s.t.} \quad & P_O - P_{\text{target}} = 0 \\ & I_{\text{ZVS}.p} + i_1(t_{S_1}) \le 0 \\ & I_{\text{ZVS}.p} - i_1(t_{S_3}) \le 0 \\ & I_{\text{ZVS}.s} - i_2(t_{Q_1}) \le 0 \\ & I_{\text{ZVS}.s} + i_2(t_{Q_3}) \le 0.\end{aligned} \tag{10}$$

Fig. 5 illustrates a comparison between the actual ac voltage gain achieved through conventional optimization techniques and the numerically optimal solution derived from (10), under varying charging voltages, powers, and ZVS currents, with the system operating in FBFB mode. It is evident that the traditional

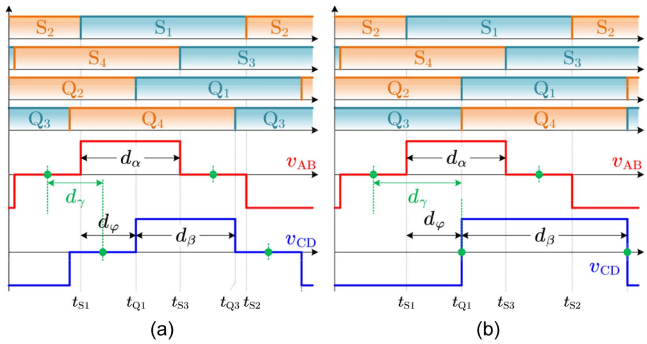

Fig. 6. Driving signals and the key waveforms of v_{AB} and v_{CD} (a) DPS modulation (b) EPS modulation.

approach does not maintain a constant ac voltage gain of one due to the constraints imposed by control variable bounds—for instance, the limitation of d_β to 0.5—and the integration of ZVS conditions. Furthermore, there is a notable discrepancy between the conventional method and the theoretical optimal solution, particularly within the medium-voltage range. This discrepancy highlights the potential for enhancing conventional optimization strategies from the standpoint of voltage gain.

B. PSM Principle and Its Simplification

In this article, the FBFB mode is presented solely as an exemplar. Nonetheless, other configurations such as FBHB, HBFB, and HBHB mode are subject to the same constraints and are equally amenable to the proposed methodology.

If no restrictions are placed on d_α, d_β, and d_γ, that is known as TPS modulation, which is a three degree of freedoms modulation strategy and it is hard to find the coupling relationship with refined ZVS implementation among each free control variable in practical applications. If make $d_\alpha = d_\beta$ or $d_\beta = 0.5$, the TPS modulation is transformed into dual-phase-shift (DPS) modulation and EPS modulation strategies as for the dual-active-bridge converter in conductive charging system, whose key waveforms are plotted in Fig. 6, and the control degrees of freedom are reduced from three to two and make the implementation simpler.

In Fig. 6, d_φ is the phase difference between the rising edges of v_{AB} and v_{CD}, as well as the driving phase difference between S_1 and Q_1, which satisfies the following relationship with the fundamental phase ratio d_γ

$$d_\gamma = d_\varphi + \frac{1}{2}(d_\beta - d_\alpha). \tag{11}$$

Since DPS and EPS are special cases of TPS, the properties of the IPT system under TPS can be converted to those of DPS and EPS by the following settings and distinguished by subscripts, such as $i_{1.\,\mathrm{DPS}}$, $i_{1.\,\mathrm{EPS}}$, $P_{O.\,\mathrm{DPS}}$, $P_{O.\,\mathrm{EPS}}$, etc

$$\text{DPS}: \ d_\beta = d_\alpha$$

$$\text{EPS}: \ d_\beta = 0.5.$$

Fig. 7 plots the comparison of the optimal numerical solutions between TPS, DPS, and EPS with different values of k and V_2 under FBFB mode, where the optimization problem is defined in (10). These data were obtained using the nonlinear programming toolbox in MATLAB. It can be seen that regardless of the value of k, the role of the TPS can be completely replaced by the EPS un-der low voltage conditions and by DPS under high voltage conditions. As a result, the modulation strategy can be simplified, and the output power is only regulated by the free control variable d_α and d_γ (or d_φ). However, different combination sets of the free control variables may result in different current stresses and switching characteristics while the output power is identical, which needs to be optimized further.

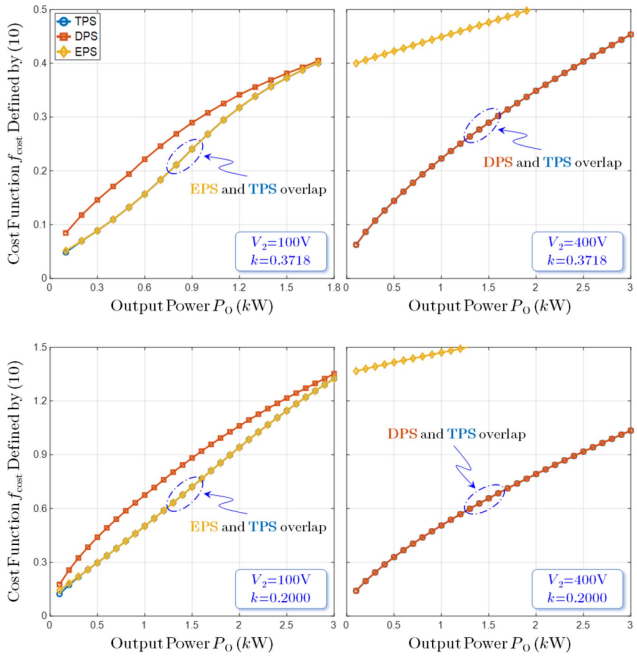

Fig. 7. Comparisons between TPS, DPS, and EPS under FBFB mode.

C. Generation of the Control Set

The Karush–Kuhn–Tucker conditions suggest that the optimal solution pertaining to (10) typically adheres to one or several inequality constraints precisely, thereby reducing the analytical complexity by transforming these inequality constraints into equality constraints. Numerical solution analysis indicates that the IPT system achieves ZVS of certain switches with minimal ZVS current across various operational conditions (as depicted in Fig. 8, wherein the red solid line demarcates the boundary between EPS and DPS modes). This demonstrates that the optimal solution derived from the optimization problem formulated in (10) can be feasibly tracked in real-time provided that these five scenarios are encountered.

Case 1: According to the analysis of the optimal numerical solution, it is found that the system works in DPS mode in this case, and when the ZVS condition of S_1 is activated, the ZVS conditions of other switches can be automatically satisfied. That is, the ZVS constraints of S_3, Q_1, and Q_3 are not activated. Therefore, the optimization problem can be simplified as

$$\min \quad f_{\text{cost}} = i_{1.\text{RMS}}^2 + i_{2.\text{RMS}}^2$$

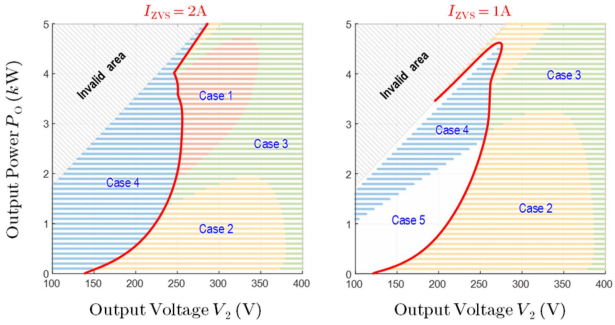

Fig. 8. Distribution regions of each case of optimal numerical solution.

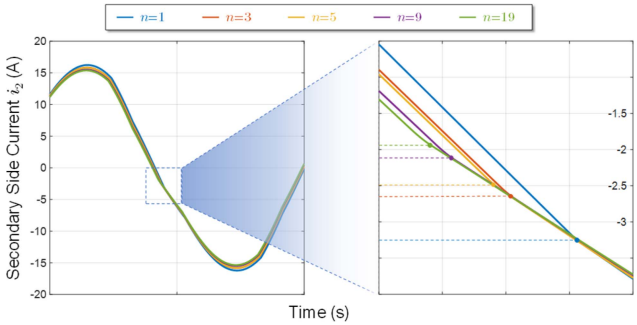

Fig. 9. Accuracy of the ZVS current tracking on the secondary side considering different order harmonics when $I_{ZVS} = 2$ A.

$$\text{s.t.} \quad P_O - P_{\text{target}} = 0$$
$$I_{ZVS.p} + i_1\ (t_{S_1}) = 0. \tag{12}$$

It is evident that the four inequality constraints have been reduced to one equality constraint, thereby simplifying the complexity of theoretical analysis and derivation.

Subsequently, based on (2) and (3), along with $I_{ZVS.p} + i_1\ (t_{S_1}) = 0$, and employing Taylor's first-order approximation, the relationship required for the external phase shift ratio in this case can be deduced, as follows:

$$d_\gamma \approx \frac{V_{ZVS} + \frac{4kV_1}{\pi}\sum_{n=3}^{\infty}\frac{(n^2-1)\sin^2(n\pi d_\alpha)}{k^2n^4-(n^2-1)^2}}{8V_2\sin(\pi d_\alpha)} - \frac{1}{2}d_\alpha$$
$$\triangleq d_{\gamma.\text{DPS}.S1} \tag{13}$$

where $V_{ZVS} = I_{ZVS}\,\omega_S L_m$.

Other cases can be analogously derived, so they will not be elaborated here.

Case 2: the system works in DPS mode, and Q_3 is turned ON at the minimum ZVS current I_{ZVS}

$$d_\gamma \approx \frac{V_{ZVS} - \frac{4kV_2}{\pi(1-k^2)}\sum_{n=3}^{\infty}\frac{\sin^2(n\pi d_\alpha)}{n^2}}{8V_1\sin(\pi d_\alpha)} - \frac{1}{2}d_\alpha$$
$$\triangleq d_{\gamma.\text{DPS}.Q3}. \tag{14}$$

Case 3: The system works in DPS mode, and S_1 and Q_3 are both turned ON at the minimum ZVS current I_{ZVS}. The solution of d_γ satisfies both (13) and (14).

Case 4: The system works in EPS mode, and S_1 is turned ON at the minimum ZVS current I_{ZVS}

$$d_\gamma \approx \frac{V_{ZVS} + \frac{4kV_1}{\pi}\sum_{n=3}^{\infty}\frac{(n^2-1)\sin^2(n\pi d_\alpha)}{k^2n^4-(n^2-1)^2}}{8V_2} - \frac{1}{2}d_\alpha$$
$$\triangleq d_{\gamma.\text{EPS}.S1}. \tag{15}$$

Case 5: The system works in EPS mode, but none of the ZVS constraints are activated. The value of d_γ is consistent with the traditional method

$$d_\gamma \approx -\frac{1}{2}d_\alpha \triangleq d_{\gamma.\text{EPS.None}}.302 \tag{16}$$

By analyzing the numerical solution of the control trajectory, it can be seen that the external phase shift angles of the DPS and EPS modes should satisfy the following relationship:

$$\begin{cases} d_{\gamma.\text{DPS}} = \max\left(d_{\gamma.\text{DPS}.S1}, d_{\gamma.\text{DPS}.Q3}\right) \\ d_{\gamma.\text{EPS}} = \max\left(d_{\gamma.\text{EPS}.S1}, d_{\gamma.\text{EPS.None}}\right) \end{cases}. \tag{17}$$

Therefore, to ensure the ZVS of the system in the discussed range of operating conditions, the external phase shift angle needs to comply with the following equation:

$$d_\gamma = \begin{cases} d_{\gamma.\text{DPS}} & f_{\text{cost.DPS}} \le f_{\text{cost.EPS}} \\ d_{\gamma.\text{EPS}} & f_{\text{cost.DPS}} > f_{\text{cost.EPS}} \end{cases}. \tag{18}$$

Another control variable, d_α, can be automatically generated by the PI regulator because it is positively related to P_O.

Fig. 9 illustrates the tracking accuracy of the ZVS currents at the secondary side as an example when different order harmonics are considered at $I_{ZVS} = 2$ A. It can be seen that the fewer the harmonics orders considered, the higher the current amplitude (and RMS current) and the higher the error in the ZVS current. In fact, $n = 9$ and $n = 19$ have similar effects.

D. Working Mode Identification and Control Scheme

The following section has discussed the principles of d_γ in different cases in detail, but another critical problem is the identification of the boundary between DPS and EPS modes. The usual idea is to compare the values of f_{cost} of both modes with the same P_O, however, even from the fundamental analysis perspective, it is not feasible because of its complexity. The reverse thinking, i.e., the principle of having a larger P_O for the same f_{cost} to determine the operating mode, is much simpler. Therefore, by making $f_{\text{cost.DPS}.1} = f_{\text{cost.EPS}.1}$ (the first component of f_{cost} for DPS and EPS modes, respectively, whose accuracy has been verified to be sufficient to characterize the final target), the relationship between $d_{\alpha.\text{DPS}}$ and $d_{\alpha.\text{EPS}}$ with the same f_{cost} is solved as

$$d_{\alpha.\text{EPS}} = \frac{\arcsin\left[\sqrt{(1+G_{\text{DC}}^2)\sin^2(\pi d_{\alpha.\text{DPS}}) - G_{\text{DC}}^2}\right]}{\pi}. \tag{19}$$

Therefore, if the value of $d_{\alpha.\text{DPS}}$ is given, the value of $d_{\alpha.\text{EPS}}$ for the same value of f_{cost} can be then derived as per (19).

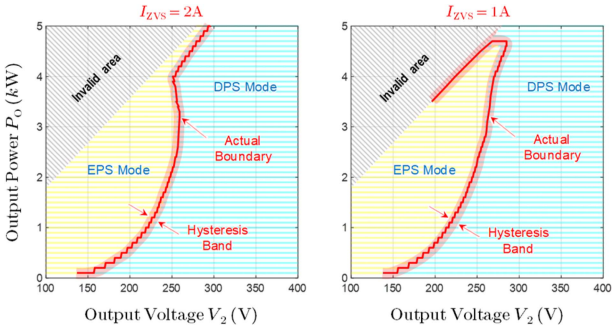

Fig. 10. Boundary identification of DPS and EPS modes.

TABLE I
PSEUDOCODE OF THE OPERATING MODE IDENTIFICATION

Step	Actions
1	generate the value of $d_{\alpha.\mathrm{DPS}}$ by the PI controller;
2	if (20) is real
3	working in DPS mode;
4	else
5	calculate the value of $d_{\alpha.\mathrm{EPS}}$ by (19) under the same f_{cost};
6	calculate the $d_{\gamma.\mathrm{DPS}}$, $P_{\mathrm{O.DPS}}$ of DPS mode by $d_{\alpha.\mathrm{DPS}}$;
7	calculate the $d_{\gamma.\mathrm{EPS}}$, $P_{\mathrm{O.EPS}}$ of EPS mode by $d_{\alpha.\mathrm{EPS}}$;
8	calculate the power difference $P_{\mathrm{diff}}=P_{\mathrm{O.EPS}}-P_{\mathrm{O.DPS}}$;
9	if $P_{\mathrm{diff}}>0$
10	working in EPS mode;
11	else
12	working in DPS mode;
13	end
14	end

Sustituting $d_{\alpha.\mathrm{DPS}}$ and $d_{\alpha.\mathrm{EPS}}$ to the power expression, the values of $P_{O.\mathrm{DPS}}$ and $P_{O.\mathrm{EPS}}$ can be attained, and their difference at the same f_{cost} is defined as

$$P_{\mathrm{diff}}=P_{O.\mathrm{EPS}}\ -P_{O.\mathrm{DPS}}.$$

Since $d_{\alpha.\mathrm{EPS}}$ is a real value, the following equation needs to be satisfied:

$$\left(1+G_{\mathrm{DC}}^2\right)\sin^2\left(\pi d_{\alpha.\mathrm{DPS}}\right)-G_{\mathrm{DC}}^2\geq 0. \tag{20}$$

Fig. 10 plots the distribution of the working areas of the DPS and EPS modes and their boundaries, where the yellow area works in the EPS mode, the cyan area works in the DPS mode, and the red solid line is the actual mode boundary obtained by using the above method. It is easy to see that there is only a very small difference between the actual boundary and the theoretical boundary. In order to avoid the system switching the working mode frequently near the boundary, a hysteresis working band can usually be set up, as shown in the red shaded part of Fig. 8. Summarizing the above two reasons, the working mode boundary identification method proposed above can ignore the error between the theoretical boundary and the actual boundary, i.e., the proposed method is feasible.

To conclude, the pseudocode of the operating mode identification is given in Table I, and the control block diagram is shown in Fig. 11. In Fig. 11, $V_{2.\mathrm{ref}}$ is the reference value of the output voltage, its difference with v_2 is used as the input of the PI regulator to create $d_{\alpha.\mathrm{DPS}}$ automatically. After that, the identification

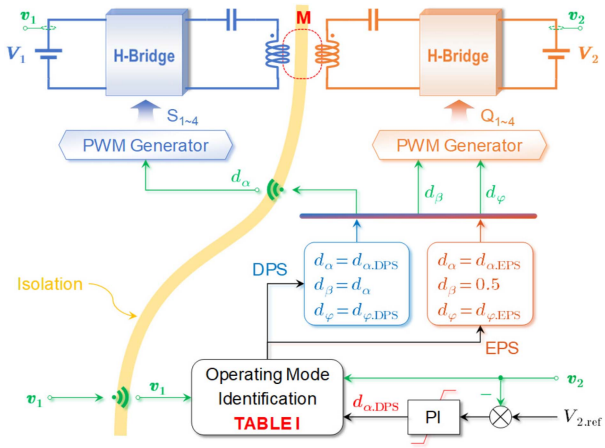

Fig. 11. Control block diagram.

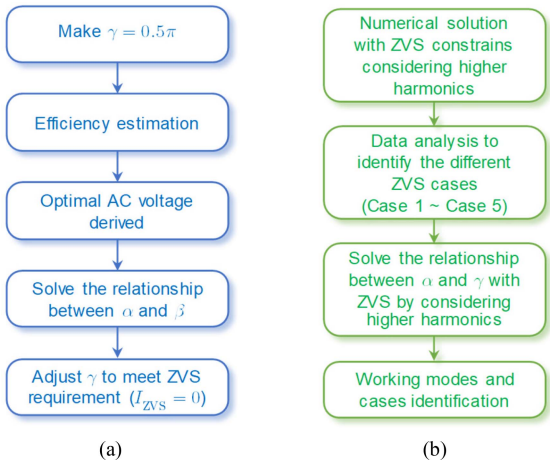

Fig. 12. Comparison of the optimization processes for different methods (a) traditional method (b) proposed method.

of the operating modes is performed according to Table I and the corresponding control variables are generated and injected into the PWM generator to drive the primary and secondary bridge legs to act as required according to the definitions of DPS mode and EPS mode. Fig. 12 summarizes the difference in the operation process between the traditional method and the proposed method. Table II given the horizontal-comparison of different control methods.

If the ac voltage gains of the optimal TPS, traditional method, and improved method are defined as $G_{\mathrm{AC.opt}}$, $G_{\mathrm{AC.trad}}$, and $G_{\mathrm{AC.pro}}$, respectively, then the ac voltage gain deviation can be defined as

$$G_{\mathrm{AC.diff}}=\left(G_{\mathrm{AC.trad}}-G_{\mathrm{AC.opt}}\right)\ -\left(G_{\mathrm{AC.pro}}-G_{\mathrm{AC.opt}}\right).$$

Since the EPS mode can be interchanged with the traditional method, Fig. 13 illustrates the 3-D surface of $G_{\mathrm{AC.diff}}$ under DPS mode. It can be seen that $G_{\mathrm{AC.diff}}$ is greater than zero for the vast majority of working conditions within the operating area. This indicates that the deviation between the traditional method and the optimal ac voltage gain is larger than the deviation between

TABLE II
HORIZONTAL-COMPARISON OF DIFFERENT CONTROL METHODS

	Compensation	Rectifier	Modulation Strategy	Analysis Model	ZVS Current is Considered	Voltage Width	Control Complexity
[19]	S-S	Passive	PFM+SPS	FHA	No	1.22	★★★
[20]	S-S	Passive	SPS	FHA	\	1.67	★
[21]	S-S	Semi-Active	2-PSM	FHA	\	1.00	★★
[22]	S-S	Active	TPS	FHA	\	1.00	★★
[23]	S-S	Active	TPS	FHA	No	2.67	★★★
[24]	S-S	Active	EPS	FHA	No	2.25	★
[25]	LCC-LCC	Active	TPS	FHA	No	1.50	★
[26]	S-S	Active	TPS	FHA	Yes	1.42	★
[27]	S-S	Active	TPS	FHA	No	1.00	★★
[28]	S-S	Active	TPS	FHA	No	1.00	★★
[29]	S-S	Active	TPS	FHA	No	2.67	★★
Proposed	S-S	Active	EPS + DPS	HHA	Yes	4.00	★★

Note: 2-PSM (Two-degree-of-freedom PSM); FHA (Fundamental Harmonic Analysis); HHA (Higher Harmonic Analysis); Voltage Width (the ratio of maximum voltage gain to minimum voltage gain); The more ★, the more complex it represents.

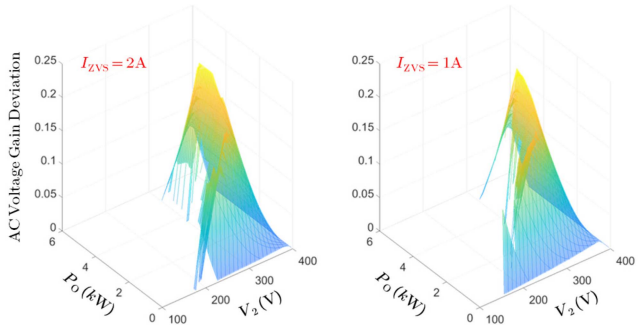

Fig. 13. AC voltage gain deviation comparison.

TABLE III
SYSTEM SPECIFICATIONS

Components	Parameters
Input Voltage (V_1)	400 V
Output Voltage (V_2)	100 V ~ 400 V
Peak Power (P_O)	1.0 kW
Switching Frequency (f_S)	85 kHz
Self-Inductance (L_1, L_2)	92.1 μH, 93.4 μH
Mutual Inductance (M)	34.25 μH
Compensation Capacitance (C_1, C_2)	37.34 nF, 37.95 nF
Primary Side Resistance (R_{L1} + R_{C1})	220.71 mΩ
Secondary Side Resistance (R_{L2} + R_{C2})	207.48 mΩ
Resistance of MOSFETs ($R_{DS,ON}$)	80 mΩ

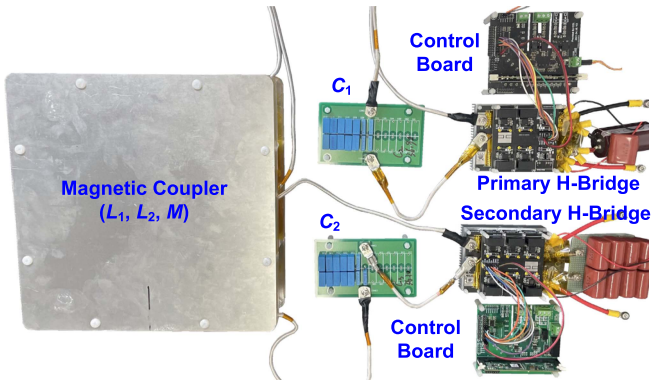

Fig. 14. Photograph of the small-scale prototype.

the proposed method and the optimal ac voltage gain, revealing that the proposed method indeed can narrow the gap with the optimal voltage gain.

During the control process, d_α needs to be passed to the primary side via wireless communication, and V_1 is usually a constant value or a slowly varying voltage, which also needs to be passed to the secondary side via wireless communication. The signal synchronization strategy for bilateral can be implemented by the method introduced in [26] and [28], which is not discussed in detail as it is out of the scope of this article. The goal of this article is to exploit the efficiency potential ignored by traditional optimization method. It should be re-emphasized that the ideas of the solution process proposed in this article are applicable to other modes such as FBHB, HBFB, and HBHB.

IV. EXPERIMENTAL VERIFICATIONS

A. Prototype

A 1.0 kW experimental prototype is built to verify the effectiveness of the proposed online tracking method. The photograph of the prototype is shown in Fig. 14. The power circuits are covered by the driver boards. The system specifications are given in Table III.

B. Experimental Results

In the experiments, only harmonic components up to the 19th order are considered in order to reduce the computational load on the DSP. The control period is $3 \cdot T_S$. Also, to highlight the realization of ZVS, set $I_{ZVS} = 2$ A. Figs. 15 and 16 show the steady-state experimental results for different input voltages at different loads. The results show that the system can operate reliably within the full power and voltage range by employing the proposed method. It can also be seen that ZVS is achieved for each operating condition, i.e., the currents corresponding to each rising and falling edge of v_{AB} and v_{CD} satisfy the ZVS requirements, but the presence of the dead time inevitably leads to some deviation.

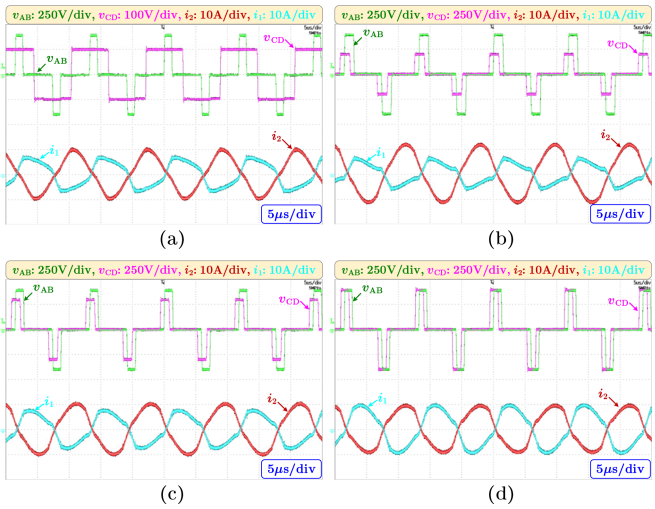

Fig. 15. Steady-state results at different output voltages under 0.2 kW (a) V2 = 100V, Po = 0.2kW (b) V2 = 200V, Po = 0.2kW (c) V2 = 300V, Po = 0.2kW (d) V2 = 400V, Po = 0.2kW.

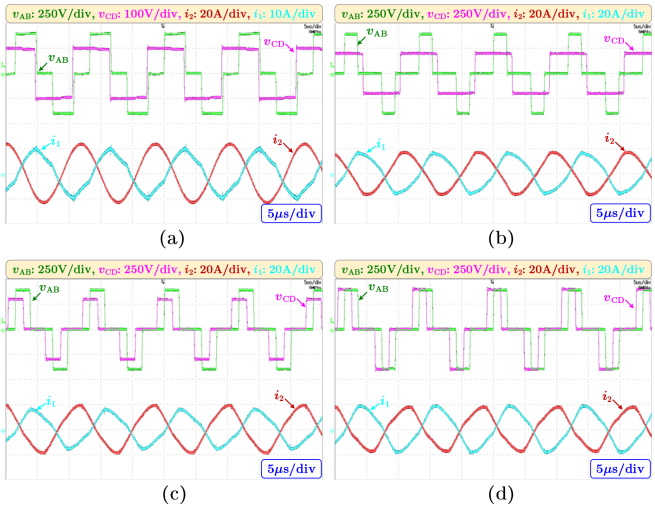

Fig. 16. Steady-state results at different output voltages under 1.0 kW (a) V2 = 100V, Po = 1.0kW (b) V2 = 200V, Po = 1.0kW (c) V2 = 300V, Po = 1.0kW (d) V2 = 400V, Po = 1.0kW.

Referring to Fig. 10, the working mode will shift between EPS and DPS when the load is switched across a certain range. To demonstrate the effectiveness of mode shifting, Fig. 17 provides the dynamic response result conducted at $V_2 = 200$ V. Fig. 17(a) shows the load switching from 0.6 to 0.8 kW, and the corresponding mode is shifting from EPS to DPS. Fig. 17(b) shows the opposite. The results indicate that the system can return to stability within a relatively short period of time after load switching. In addition, at the moment of load switching, the drop or overshoot of the voltage and current is acceptable.

From the steady-state and dynamic experiments, it is known that although the control equations of the proposed method become more complicated, the arithmetic power of the DSP is still able to support it.

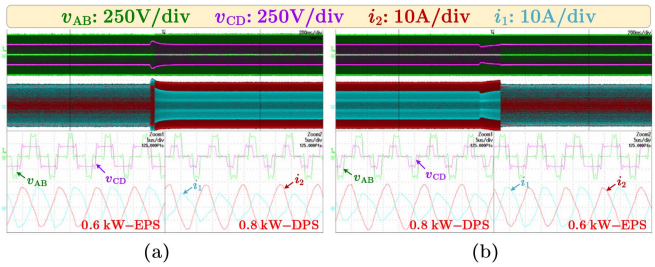

Fig. 17. Dynamic response at $V2 = 200$ V (a) EPS to DPS (b) DPS to EPS.

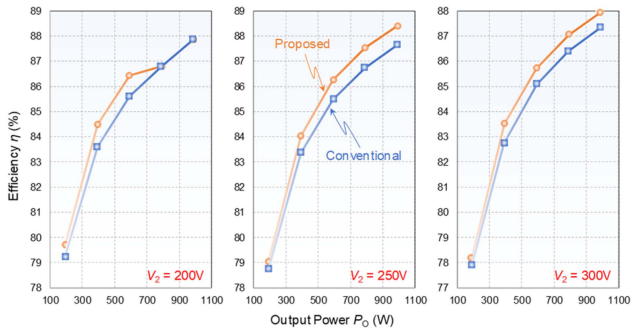

Fig. 18. Measured efficiency of different methods.

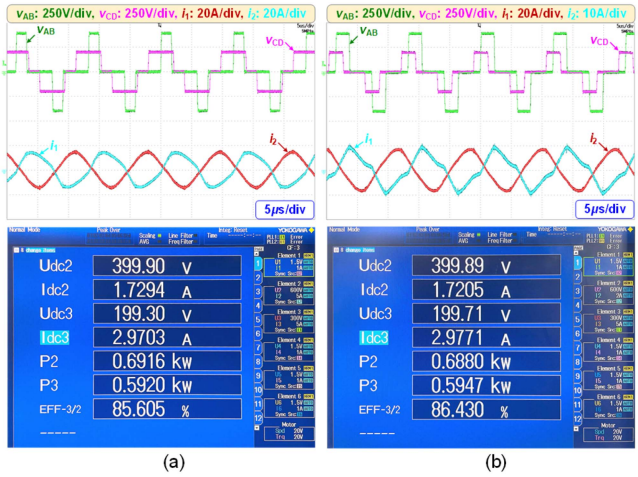

Fig. 19. Comparison of waveforms between traditional and proposed methods ($V_2 = 200$ V and $P_O = 600$ W) (a) traditional method (b) improved method.

Fig. 18 provides the conversion efficiency measured by the power analyzer WT1800 supported by YOKOGAWA by utilizing the proposed method and the traditional method at different voltages and loads. From Fig. 5, it can be seen that the optimal ac voltage gain difference between the traditional method and the proposed method is in the medium voltage and medium load, so this article only compares these working conditions. The conditions for comparing tests were completely consistent, with no modifications or adjustments to the hardware circuit and testing equipment; the differences lie solely in control strategies.

Fig. 19 shows the waveform comparison of the proposed method and the traditional method at $V_2 = 200$ V and $p_O = 600$ W. It should be noted that the scale of i_2 in Fig. 19 is

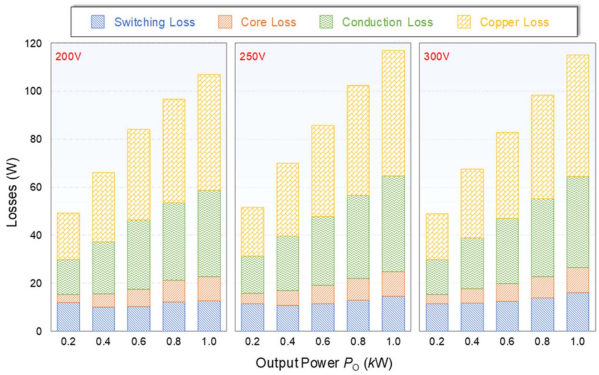

Fig. 20. Loss breakdown analysis.

inconsistent (20 A/div for the traditional method and 10 A/div for the proposed method). It can be seen from the figure that the improved method significantly reduces d_β compared to the traditional method, thereby reducing the RMS value of i_1. Comparing the waveforms of i_1 of both methods also shows that, compared to the traditional method, the current waveform of the improved method has a larger notch, and its RMS value is reduced by about 44.36%. For d_α, the proposed method slightly increases compared to the traditional method, resulting in an increase in the RMS value of i_2 by about 13.27%. Overall, the current stress [defined by (10)] of the proposed method is reduced by about 21.19% compared to the traditional method. Therefore, the system efficiency can be improved.

The findings from the measurements indicate that the improvement method proposed in this article can indeed boosts the system's efficiency under these specific operating conditions. Actually, both methods inevitably harbor errors stemming from factors such as dead time and parameter drift. In this scenario, both methods achieve ZVS. Therefore, the essence of the proposed method that can improve the efficiency of the system does not lie in the realization of the ZVS, but in the adjustment of the ac voltage gain to converge to the theoretical optimum. Although in absolute numerical terms the method proposed in this article leads to a system efficiency improvement of up to only 1%, the resulting energy efficiency savings are significant with the large-scale application of high-power wireless charging technologies.

The loss breakdown analysis of the system is shown in Fig. 20 and the analyzed data is derived from the simulation results. There is a high trend match between the loss analysis and the experimental results. As can be seen from Fig. 20, the main losses are concentrated in conduction loss and copper loss (including the equivalent Equivalent Series Resistance (ESR) of the resonant capacitor). Limited by the size and area of the coupler, resulting in a matched resonant capacitor equivalent ESR cannot be reduced. This reveals the reason for the low efficiency measured for the system. However, the point of the experiment is not to seek the ultimate in system efficiency, but to verify the effectiveness of the proposed method. Therefore, the purpose of the experimental results has been achieved.

V. Conclusion

In this article, the limitations of traditional efficiency optimization methods for an S-S compensated IPT system are demonstrated through theoretical analysis and experimental verification. By analyzing the optimal numerical solution, it is pointed out that the ac voltage gain at the optimal operating point of the system when ZVS is considered cannot be a constant value, and the TPS modulation strategy can be replaced by the DPS and EPS modulation strategies. The phase shift angle offset required to realize ZVS is derived by introducing higher harmonics. Although the formulas are more complex, they are sufficiently burdened by the DSP controller. The experimental results show that the traditional method indeed has room for further optimization in some working conditions by breaking the fixed ac voltage gain constraints and considering the ZVS implementation. In general, both the traditional and the proposed methods are applicable. But, the proposed method can realize ZVS by adjusting the phase angle offset arbitrarily according to the specified ZVS currents, which improves the flexibility of the regulation strategy. When wireless charging systems are applied on a large scale, the operational economics of the proposed method for efficiency gains are extremely impressive.

References

[1] Y. Zhang, S. Chen, X. Li, and Y. Tang, "Dual-side phase-shift control of wireless power transfer implemented on primary side based on driving windings," *IEEE Trans. Ind. Electron.*, vol. 68, no. 9, pp. 8999–9002, Sep. 2021.

[2] G. Li and H. Ma, "A hybrid IPT system with high-misalignment tolerance and inherent CC–CV output characteristics for EVs charging applications," *IEEE J. Emerg. Sel. Topics Power Electron.*, vol. 10, no. 3, pp. 3152–3160, Jun. 2022.

[3] Y. Guo and Y. Zhang, "Secondary side voltage and current estimation of wireless power transfer systems," *IEEE Trans. Ind. Appl.*, vol. 58, no. 1, pp. 1222–1230, Jan./Feb. 2022.

[4] Z. Yi, M. Li, B. Muneer, G. He, and X.-X. Yang, "Self-resonant antisymmetric planar coil for compact inductive power transfer system avoiding compensation circuits," *IEEE Trans. Power Electron.*, vol. 36, no. 5, pp. 5121–5134, May 2021.

[5] Y. Zhang, S. Chen, X. Li, and Y. Tang, "Design methodology of free-positioning nonoverlapping wireless charging for consumer electronics based on antiparallel windings," *IEEE Trans. Ind. Electron.*, vol. 69, no. 1, pp. 825–834, Jan. 2022.

[6] X. Yi, W. Zheng, H. Cao, S. Wang, X. Feng, and Z. Yang, "Wireless power transmission for implantable medical devices using focused ultrasound and a miniaturized 1-3 piezoelectric composite receiving transducer," *IEEE Trans. Ultrason., Ferroelect., Freq. Control*, vol. 68, no. 12, pp. 3592–3598, Dec. 2021.

[7] Z. Yan, K. Zhang, L. Qiao, Y. Hu, and B. Song, "A multiload wireless power transfer system with concentrated magnetic field for AUV cluster system," *IEEE Trans. Ind. Appl.*, vol. 58, no. 1, pp. 1307–1314, Jan./Feb. 2022.

[8] A. Zakerian, S. Vaez-Zadeh, and A. Babaki, "A dynamic WPT system with high efficiency and high power factor for electric vehicles," *IEEE Trans. Power Electron.*, vol. 35, no. 7, pp. 6732–6740, Jul. 2020.

[9] C. Zhu et al., "Analysis and design of cost-effective wpt systems with dual independently regulatable outputs for automatic guided vehicles," *IEEE Trans. Power Electron.*, vol. 36, no. 6, pp. 6183–6187, Jun. 2021.

[10] L. He and D. Guo, "A clamped and harmonic injected class-e converter with ZVS and reduced voltage stress over wide range of distance in WPT system," *IEEE Trans. Power Electron.*, vol. 36, no. 6, pp. 6339–6350, Jun. 2021.

[11] J. Hu, J. Zhao, and C. Cui, "A wide charging range wireless power transfer control system with harmonic current to estimate the coupling coefficient," *IEEE Trans. Power Electron.*, vol. 36, no. 5, pp. 5082–5094, May 2021.

[12] W. X. Zhong and S. Y. R. Hui, "Maximum energy efficiency tracking for wireless power transfer systems," *IEEE Trans. Power Electron.*, vol. 30, no. 7, pp. 4025–4034, Jul. 2015.
[13] H.-L. Jou, J.-C. Wu, K.-D. Wu, and C.-Y. Kuo, "Bidirectional DC–DC wireless power transfer based on LCC-C resonant compensation," *IEEE Trans. Power Electron.*, vol. 36, no. 2, pp. 2310–2319, Feb. 2021.
[14] X. Zhu et al., "High-efficiency WPT system for CC/CV charging based on Double-Half-Bridge inverter topology with variable inductors," *IEEE Trans. Power Electron.*, vol. 37, no. 2, pp. 2437–2448, Feb. 2022.
[15] W. Li, Q. Zhang, C. Cui, and G. Wei, "A self-tuning S/S compensation WPT system without parameter recognition," *IEEE Trans. Ind. Electron.*, vol. 69, no. 7, pp. 6741–6750, Jul. 2022.
[16] N. Fu, J. Deng, Z. Wang, and D. Chen, "An LCC–LCC compensated WPT system with Switch-controlled capacitor for improving efficiency at wide output voltages," *IEEE Trans. Power Electron.*, vol. 38, no. 7, pp. 9183–9194, Jul. 2023.
[17] Y. Lim, H. Tang, S. Lim, and J. Park, "An adaptive impedance-matching network based on a novel capacitor matrix for wireless power transfer," *IEEE Trans. Power Electron.*, vol. 29, no. 8, pp. 4403–4413, Aug. 2014.
[18] G. Lee, B. H. Waters, Y. G. Shin, J. R. Smith, and W. S. Park, "A reconfigurable resonant coil for range adaptation wireless power transfer," *IEEE Trans. Microw. Theory Techn.*, vol. 64, no. 2, pp. 624–632, Feb. 2016.
[19] Y. Jiang, L. Wang, Y. Wang, J. Liu, M. Wu, and G. Ning, "Analysis, design, and implementation of WPT system for EV's battery charging based on optimal operation frequency range," *IEEE Trans. Power Electron.*, vol. 34, no. 7, pp. 6890–6905, Jul. 2019.
[20] Y. Li, J. Hu, F. Chen, Z. Li, Z. He, and R. Mai, "Dual-phase-shift control scheme with current-stress and efficiency optimization for wireless power transfer systems," *IEEE Trans. Circuits Syst. I, Reg. Papers*, vol. 65, no. 9, pp. 3110–3121, Sep. 2018.
[21] L. Yang, Y. Shi, M. Wang, and L. Ren, "Constant voltage charging and maximum efficiency tracking for WPT systems employing Dual-side control scheme," *IEEE J. Emerg. Sel. Topics Power Electron.*, vol. 10, no. 1, pp. 945–955, Feb. 2022.
[22] T. Tan, K. Chen, Y. Jiang, Q. Lin, L. Yuan, and Z. Zhao, "A bidirectional wireless power transfer system control strategy independent of real-time wireless communication," *IEEE Trans. Ind. Appl.*, vol. 56, no. 2, pp. 1587–1598, Mar./Apr. 2020.
[23] Y. Jiang, L. Wang, J. Fang, C. Zhao, K. Wang, and Y. Wang, "A joint control with variable ZVS angles for dynamic efficiency optimization in wireless power transfer system," *IEEE Trans. Power Electron.*, vol. 35, no. 10, pp. 11064–11081, Oct. 2020.
[24] Y. Jiang, L. Wang, J. Fang, R. Li, R. Han, and Y. Wang, "A high-efficiency ZVS wireless power transfer system for electric vehicle charging with variable angle phase shift control," *IEEE Trans. J. Emerg. Sel. Topics Power Electron.*, vol. 9, no. 2, pp. 2356–2372, Apr. 2021.
[25] X. Zhang et al., "A control strategy for efficiency optimization and wide ZVS operation range in bidirectional inductive power transfer system," *IEEE Trans. Ind. Electron.*, vol. 66, no. 8, pp. 5958–5969, Aug. 2019.
[26] F. Xu, S.-C. Wong, and C. K. Tse, "Overall loss compensation and optimization control in single-stage inductive power transfer converter delivering constant power," *IEEE Trans. Power Electron.*, vol. 37, no. 1, pp. 1146–1158, Jan. 2022.
[27] Y. Liu, U. K. Madawala, R. Mai, and Z. He, "An optimal multivariable control strategy for inductive power transfer systems to improve efficiency," *IEEE Trans. Power Electron.*, vol. 35, no. 9, pp. 8998–9010, Sep. 2020.
[28] G. Zhu, J. Dong, W. Shi, T. B. Soeiro, J. Xu, and P. Bauer, "A mode-switching-based phase shift control for optimized efficiency and wide ZVS operations in wireless power transfer systems," *IEEE Trans. Power Electron.*, vol. 38, no. 4, pp. 5561–5575, Apr. 2023.
[29] M. Li, J. Deng, D. Chen, W. Wang, and Z. Wang, "Maximum efficiency tracking and ZVS realization for wide output voltage range employing segmented tps modulation scheme," *IEEE Trans. Veh. Technol.*, vol. 72, no. 10, pp. 12770–12783, Oct. 2023.

Deliang Chen received the B.Eng. and M.Eng. degrees in electrical engineering and the Ph.D. degree in mechanical engineering from Beijing Institute of Technology, Beijing, China, in 2016, 2019, and 2023, respectively.

Since July 2023, he has been a Research Associate with the School of Electrical Engineering, Shandong University, Jinan, China. His research interests primarily focus on the topology, modulation, and control of both ac and dc power converters.